Multiphase Gas Flows in the Nearby Seyfert Galaxy ESO428–G014. Paper I

C. Feruglio[1,2] , G. Fabbiano[3] , M. Bischetti[4] , M. Elvis[3] , A. Travascio[4], and F. Fiore[1,2]
[1] INAF Osservatorio Astronomico di Trieste, Via G.B. Tiepolo, 11, Trieste, I-34143, Italy; chiara.feruglio@inaf.it
[2] IFPU—Institute for Fundamental Physics of the Universe, Via Beirut 2, I-34014 Trieste, Italy
[3] Center for Astrophysics, Harvard & Smithsonian, 60 Garden Street, Cambridge, MA 02138, USA
[4] INAF Osservatorio Astronomico di Roma, Via Frascati 33, I-00078 Monteporzio Catone, Italy
Received 2019 March 29; revised 2019 November 28; accepted 2019 December 13; published 2020 February 10

Abstract

We present ALMA 230 GHz continuum and CO(2–1) observations of the nearby Compton-thick Seyfert galaxy ESO428–G14, with angular resolution $0\rlap{.}''7$ (78 pc). CO(2–1) is distributed in clumpy spiral arms, a lopsided circumnuclear ring (CNR) with ~200 pc radius, and a transverse gas lane with size <100 pc, which crosses the nucleus and connects the two portions of the CNR. The main CO velocity gradient is consistent with a rotating disk with dynamical mass $M_{\rm dyn} = 5 \times 10^9 M_\odot$ within ~1 kpc. We detect off-plane gas motions with respect to the main disk plane which likely trace a molecular outflow with rate $\dot{M}_{\rm of} \approx 0.1$–$0.3\, M_\odot\,{\rm yr}^{-1}$, along a biconical structure with radius 700 pc. The CO outflow smoothly joins the warm molecular outflow detected in SINFONI/ Very Large Telescope data in the central 170 pc, suggesting that the outflow may cool with increasing distance. Our dynamical modeling of the inner 100 pc region suggests a warped disk or bar, and of fast gas streams which may trace an inflow toward the AGN. The inner warped disk overlaps with the most obscured, CT region seen in X-rays. There, we derive a column density $N({\rm H}_2) \approx 2 \times 10^{23}\,{\rm cm}^{-2}$, suggesting that molecular gas may contribute significantly to the AGN obscuration. Most of the hard X-ray emitting nuclear region is deprived of cold molecular gas and shows a CO-cavity. The CO-cavity is filled with warm molecular gas traced by H_2, confirming that the 3–6 keV continuum and Fe Kα emission are due to scattering from dense ISM clouds.

Unified Astronomy Thesaurus concepts: AGN host galaxies (2017); Active galactic nuclei (16); Interstellar medium (847); Galaxy kinematics (602)

1. Introduction

The nearby Seyfert galaxy ESO428–G14 ($D \sim 23.3$ Mpc, NED; which corresponds to a physical scale of 112 pc arcsec^{-1}) hosts a Compton-thick (CT) AGN (Maiolino et al. 1998; Risaliti et al. 1999), with intrinsic bolometric luminosity $L_{\rm bol,AGN} = 4.1 \times 10^{43}$ erg s^{-1} (Levenson et al. 2006). According to Fabbiano et al. (2019), the likely black hole mass in ESO 428-G014 is $(1$–$3) \times 10^7 M_\odot$, using the McConnell & Ma (2013) scaling from bulge velocity dispersion, $\sigma = 119.7$ km s^{-1}, and bulge mass, $M(K)_{\rm bulge} = 10^{9.14}\, M_\odot$ (Peng et al. 2006). The latter is inferred from the K band magnitude and assuming a mass-to-light ratio of 0.6 (McGaugh & Schombert 2014). Given this black hole mass estimate, the Eddington ratio of ESO 428-G014 is about 1%. The host galaxy of ESO428–G14 has a stellar mass of $M_* = 3.76 \times 10^{10}\, M_\odot$ and a star formation rate of SFR$_{\rm FUV} = 1.5 \times 10^{-4}\, M_\odot$ yr^{-1} estimated from the FUV luminosity (Vaddi et al. 2016). The latter is a lower limit SFR because it is not corrected for extinction at the rest frame. ESO4280-G14 is known to have a radio jet oriented approximately along the same direction as the kinematic major axis of the galaxy (Falcke et al. 1996 and references therein). According to Riffel et al. (2007), the radio jet is launched at a small inclination with respect to the plane of the disk, such that it impacts the disk and lifts up [O III] emitting gas from the galactic plane on scales of 300–600 pc in the Narrow Line Region (Falcke et al. 1996). Ionized gas, probably pushed by the radio jet, is detected in several ionized gas tracers, such as [O III] and Hα with *HST* and Gemini (Falcke et al. 1996; Riffel et al. 2007), and warm H_2 with SINFONI/Very Large Telescope (VLT) (May et al. 2018).

ESO428-G014 has been the subject of four recent papers, based on deep *Chandra* ACIS observations. Fabbiano et al. (2017, 2018a; Paper I and Paper II) detected kiloparsec-size extended regions emitting in hard X-ray (3–6 keV) continuum and Fe Kα line. Chandra high resolution imaging of the soft (<3 keV), line-dominated X-ray emission (Fabbiano et al. 2018b, Paper III) shows remarkable correspondence between high surface brightness X-ray features and the radio jet and optical line emission. Paper III also shows that in the inner circumnuclear region of ~150 parsec, the X-ray hardness ratios are larger, indicating obscuration by Compton-thick material. In this inner region, higher surface brightness extended emission is present in both hard (>3 keV) continuum and 6.4 keV iron emission line (Fabbiano et al. 2019, Paper IV).

Paper IV also reports clumpy features in the iron line emission of ESO428-G014. Questions arise about the nature of these circumnuclear hard X-ray features, whether, e.g., they are due to a nuclear disk of dense material (the torus), or to the interaction of hard AGN photons with dense molecular clouds in the nuclear outflow, responsible for the ionization cone emission. In a similar CT AGN, NGC 5643, also recently imaged with *Chandra*, a distinct X-ray feature in the 6.4 keV iron line was reported (Fabbiano et al. 2018c), corresponding with the rotating nuclear disk found with ALMA by Alonso-Herrero et al. (2018).

All these extended and complex hard X-ray features, both on kiloparsec and ~100 pc scales, require dense scattering clouds in the interstellar medium. ALMA observations of molecular gas tracers with high enough angular resolution have the potential to shed light on the cold gas and dust component in the host galaxy and in the inner nuclear region. To this aim we have checked the ALMA archive and found public data of the rest-frame 230 GHz continuum and CO(2–1) line observations of ESO428–G14, with an angular resolution of $0\rlap{.}''7$ (78 pc).

The paper is organized as follows. Section 2 presents the ALMA observational setup and data analysis. Section 3 presents observational results. In Section 4 we compare the emission from cold molecular gas and dust seen by ALMA, with the X-ray emission seen by *Chandra* in different energy bands, and discuss our results.

2. Data and Analysis

We retrieved ALMA and optical/NIR IFU VLT data from the respective archives, as described below. We also used archival *Chandra* data, as analyzed in Paper III.

2.1. ALMA

We retrieved data of ESO428–G14 from the ALMA archive (program ID 2015.1.00086.S). These are band 6 observations acquired with the 12 m array during 2016 May, in the frequency ranges 228–232 and 242.6–246.6 GHz, which cover the CO(2–1) line and the underlying 1.3 mm continuum. The antenna primary beam size at 229.24 GHz is $\sim 25''$. The data have maximum spectral resolution of 2.5 km s^{-1}. Observation time, including overheads, was 29 minutes. We created the calibrated measurement set under software CASA (McMullin et al. 2007). We then converted it into a visibility table in GILDAS format, and we imaged the data using Mapping (Guilloteau & Lucas 2000). To obtain the continuum map, we first averaged the visibilities combining the four available spectral windows and excluding the range set by the CO(2–1) sky frequency plus/minus 300 km s^{-1}, to stay in the spectral region free from the emission line. We then imaged the continuum visibilities by adopting a natural weighting scheme, and produced a clean cube by using the mx cleaning algorithm down to a detection threshold 0.5 times the rms noise. This way we obtain a synthesized beam of $0''76 \times 0''69^2$ at a PA = 58°. The reached rms noise in the clean map is 0.027 mJy/beam in the continuum in the aggregated bandwidth. We also deconvolved using the MRC cleaning algorithm (Wakker & Schwarz 1988) to highlight multiscale emission. We obtain consistent results between mx and MRC. To obtain the continuum-subtracted visibilities of the CO(2–1) line, we subtracted the continuum in the *uv*-plane from the visibility set using the task *uv*-subtract within GILDAS. We then imaged the CO(2–1) visibilities using a natural weighting scheme with detection threshold 0.5 times the noise, reaching an rms noise level of 1.25 mJy/beam in 2.5 km s^{-1} wide channels after cleaning, and a synthetic beam of $0''8 \times 0''67^2$ FWHM at PA = 36°. The data cubes were corrected for the attenuation pattern of the primary beam.

In order to better map the inner compact region, we produced also a CO(2–1) data cube with enhanced angular resolution. We used two techniques. First, we imaged and deconvolved applying Robust weighting within GILDAS, and obtained a synthetic beam of $0.57 \times 0''53$ FWHM at PA = 55 and a rms 5.8×10^{-4} Jy/beam per 2.5 km s^{-1} channel. The second method consists in further enhancing the angular resolution by restoring with a clean beam size of $0.4 \times 0''4$, chosen to approximately match the *Chandra* point-spread function (PSF; super-resolution). We derived for this map an rms noise of 5.8×10^{-4} Jy/beam per 2.5 km s^{-1} channel. Super-resolution can break the flux estimation. For our case we checked that flux densities in the super-resolution map agrees within 15%–20% with those of the robust weighted images.

2.2. MUSE and SINFONI

We analyzed MUSE@VLT archival data of ESO428–G14. The MUSE data were calibrated with the standard pipeline. We then used the tool *CubeBKGSub* within the CubExtractor software (Borisova et al. 2016) to first estimate and subtract the stellar continuum underlying the emission line of interest, which in this case is [O III] λ5007 Å. The angular resolution of MUSE data, as estimated from the PSF, is $1''2$. Then we used *CubEx* and *Cub2Im* to create a 3D mask and the first moment of the [O III] flux distribution.

We also retrieved SINFONI@VLT data from the ESO archive. We used the *K*-band data published in May et al. (2018) to obtain a map of the H$_2$ 1−0 S(1) emission line at 2.12 μm. The angular resolution of SINFONI data is $0''2$ (May et al. 2018). For the purpose of this work, we limit the analysis to the [O III] λ5007 Å and H$_2$ 2.12 μm emission lines. A complete analysis of the MUSE and SINFONI data including several emission lines will be presented in a separate publication (C. Feruglio et al. 2020, in preparation).

3. Results

3.1. Circumnuclear Region

Figure 1 shows the 1.3 mm continuum and CO(2–1) mean-flux maps. In this and in all following maps the origin of coordinates is set to the phase tracking center of the observations, [R.A., decl.] = [07:16:31.2, −29:19:29.0], which is the position of the AGN according to Evans et al. (2010). The continuum flux density shows a peak at [R.A., decl.] = [07:16:31.2, −29:19:28.8], consistent with the AGN position from Fabbiano et al. (2018b; Paper III), and shows spatially resolved emission over a region about $5''$ wide, along the southeast to northwest direction. We measure a 1.3 mm continuum flux density of $S_{1.3mm} = 3.10 \pm 0.03$ mJy within the regions above 2σ (Figure 1).

CO(2–1) emission is detected toward the nucleus and in the circumnuclear regions of the host galaxy, out to distances of about 1 kpc from the AGN. The ALMA map reveals clumpy spiral arms that converge to arc-like structures, which may be identified with a circumnuclear ring (CNR) located at a projected radius of about $2''$, and a transverse (equatorial) gas lane which crosses the nucleus and connects the two portions of the CNR. Spiral arms and portions thereof are visible at the outskirts of the map. The brightest CO(2–1) emission is detected toward a bright clump of gas located about 230 pc north of the AGN (Figure 1, right panel), which constitutes part of the CNR. Continuum emission is also detected at the position of these ark-like structures.

We measure an integrated flux density of $S_{CO} = 63.3 \pm 0.1$ Jy km s^{-1} over a line width of 300 km s^{-1}, by integrating the flux density within the regions above 2σ in Figure 1. This translates into a line luminosity L' CO=2.1×10^7 K km s^{-1} pc^2. We assume thermalized optically thick CO emission ($L'CO_{(1-0)} = L'CO_{(2-1)}$), and adopt a luminosity-to-mass conversion factor $\alpha_{CO} = 3.2 M_\odot$ [K km s^{-1} pc^2]$^{-1}$ (Saintonge et al. 2011; Accurso et al. 2017). This translates into a molecular gas mass of $M(H_2) = 6.7 \times 10^7 (\alpha_{CO}/3.2) M_\odot$ within the inner ~ 1 kpc radius region.

Figure 2 shows maps in velocity channels 5 km s^{-1} wide, covering the whole CO(2–1) line width. The gas with blueshifted velocity is mainly located at the northwest side of
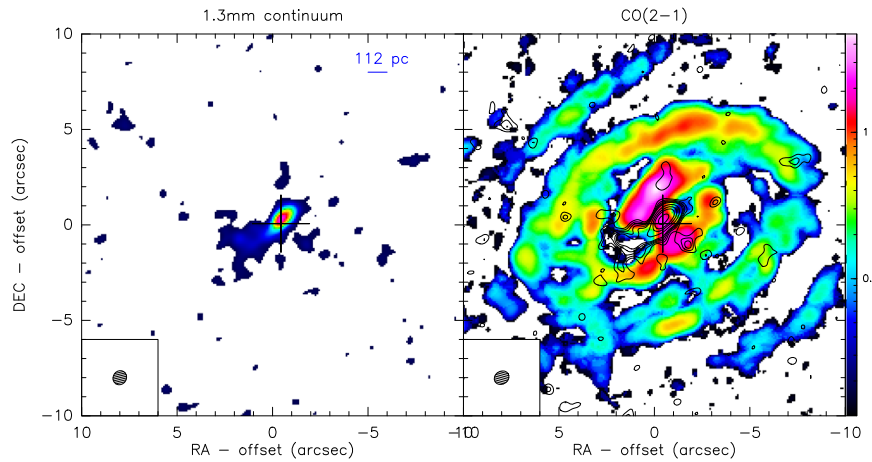
Figure 1. Left panel: the 1.3 mm continuum map of ESO428–G14. Regions with emission below 2σ have been blanked ($\sigma = 0.027$ mJy/beam). The physical scale 112 pc/" is indicated in the label. The coordinates are relative to the phase tracking center set at [R.A., decl.] = [07:16:31.2, −29:19:29.0], which is the AGN position according to Evans et al. (2010). Right panel: the CO(2–1) mean-flux (moment 0) map. The color bar is in units of Jy/beam km s^{-1}. A detection threshold of 3.5σ has been applied to produce the map. The black contours show the 1.3 mm continuum emission (contours are drawn at 2, 3, 5, 10, 15, 20σ). The synthesized beam, $0.8 \times 0''\!.67$ FWHM, is shown in the insets.

the nucleus, the redshifted one at the southeast side, along a position angle PA $\sim 35°$ (PA is defined positive from east, increasing counterclockwise). This defines the kinematic major axis of the galaxy. We detect also deviations from the main velocity gradient at a velocity of about -105 ± 10 km s^{-1} on the southeast side, and velocity 129 ± 5 km s^{-1} on the northwest side.

Figure 3 shows the CO(2–1) moment 0, 1, and 2 maps (mean-flux, velocity, and velocity dispersion, $\sigma_{\rm disp}$). The data resolve a velocity gradient with a total range of ~ 250 km s^{-1} from northwest to southeast along a PA $\sim 35°$. The velocity dispersion $\sigma_{\rm disp}$ is resolved across the galaxy and is in the range of 10–60 km s^{-1}. The $\sigma_{\rm disp}$ shows the largest value toward the nucleus, and reaches about 50 km s^{-1} in the CNR. There are also regions of enhanced $\sigma_{\rm disp}$ at large distances from the nucleus, distributed in clumps along PA = 45 and 60°, approximately in the direction of the ionization cone and radio jets. Elsewhere in the outer spiral arms, $\sigma_{\rm disp} \sim 10$ km s^{-1}.

We used the $^{\rm 3D}$BAROLO code (Di Teodoro & Fraternali 2015) to model the large-scale CO(2–1) kinematics, in order to reconstruct the rotation curve and estimate the intrinsic velocity dispersion of the disk. This is implemented by fitting 3D tilted-ring models to the emission-line data cube. As first guess parameters, we input the PA of the observed velocity gradient, 35°, and the inclination of the disk $i = 58°$, derived from the minor/major axis ratio (NED). This procedure yields the model mean-intensity, velocity, and velocity dispersion maps shown in Figure 3, bottom panels. We computed the residual velocity map by subtracting the mean-velocity model from the data (Figure 3, lower right panel). We find that the best fit disk model has inclination $i = 60 \pm 5°$, and circular velocity $v_{\rm rot} = 135 \pm 5$ km s^{-1}. This model accounts for most of the emission seen in the disk and circumnuclear regions, however the residual velocity map shows significant red- and blueshifted emission in a biconical region oriented approximately in the same PA as the kinematic major axis of the galaxy, and out to projected distances of $6''\!.5$ from the nucleus (physical scale of about 700 pc). Figure 4 shows the rotation velocity $v_{\rm rot}$ versus the radius of the best-fit disk model. We find that $v_{\rm rot}$ increases

from the center outwards, shows a peak at radii $2''$–$4''$, and then reaches a plateau at 135 km s^{-1} further out in the disk.

Figure 5 shows position–velocity diagrams cut along different PA, chosen to capture the main kinematic components seen in Figure 3. The PV diagrams are slices taken through the continuum peak position (=AGN position) and using a slit $0''\!.9$ wide, approximately the size of the synthetic beam. The PV diagram along the kinematic major axis (PA = 35°) shows projected velocity consistent with the rotating disk model (indicated with black solid points). In addition, we detect apparent counter-rotation of gas along all examined position angles (along PA = 35, 45, 60°), located both in the inner $1''$ and out to offsets of $\pm(7''$–$10'')$. As counter-rotation of the gas on the same physical scales as the main disk is unphysical, we interpret these off-plane motions as a CO outflow. The outflow velocity is comparable to the rotation velocity of the disk, besides being also oriented approximately along the major kinematic axis, which makes it challenging to separate cleanly the two components.

We subtract the $^{\rm 3D}$BAROLO CO(2–1) model cube from the clean CO(2–1) data cube, to obtain the residual (i.e., $data - model$) CO(2–1) line intensity cube. This residual cube contains the residual CO(2–1) emission after subtraction of the disk rotation model. We use it to image the CO outflow, to extract the corresponding spectral features, and to quantify its luminosity and mass. In Figure 6, left panel, we show the velocity-integrated CO(2–1) outflow map as extracted from the residual data cube. Redshifted CO(2–1) outflow emission (indicated by red contours) is found mainly on the southeast side of the nucleus, whereas blueshifted CO(2–1) outflow (blue contours) is located on the northwest side. However, faint redshifted CO emission is detected also on the northwest side, and conversely CO with blueshifted emission is seen on the southeast side, indicating that we are probably seeing both the receding and approaching side of each outflowing cone. By fitting the spectra with Gaussian functions, we find that the red peaks at a projected velocity of $v_{\rm red} = 137 \pm 1$ km s^{-1}, and the blue at $v_{\rm blue} = -87 \pm 0.2$ km s^{-1}. We derive integrated flux densities of $Sdv_{\rm red} = 2$ Jy km s^{-1} and $Sdv_{\rm blue} = 3.8$ Jy km s^{-1}. These correspond to line luminosities of
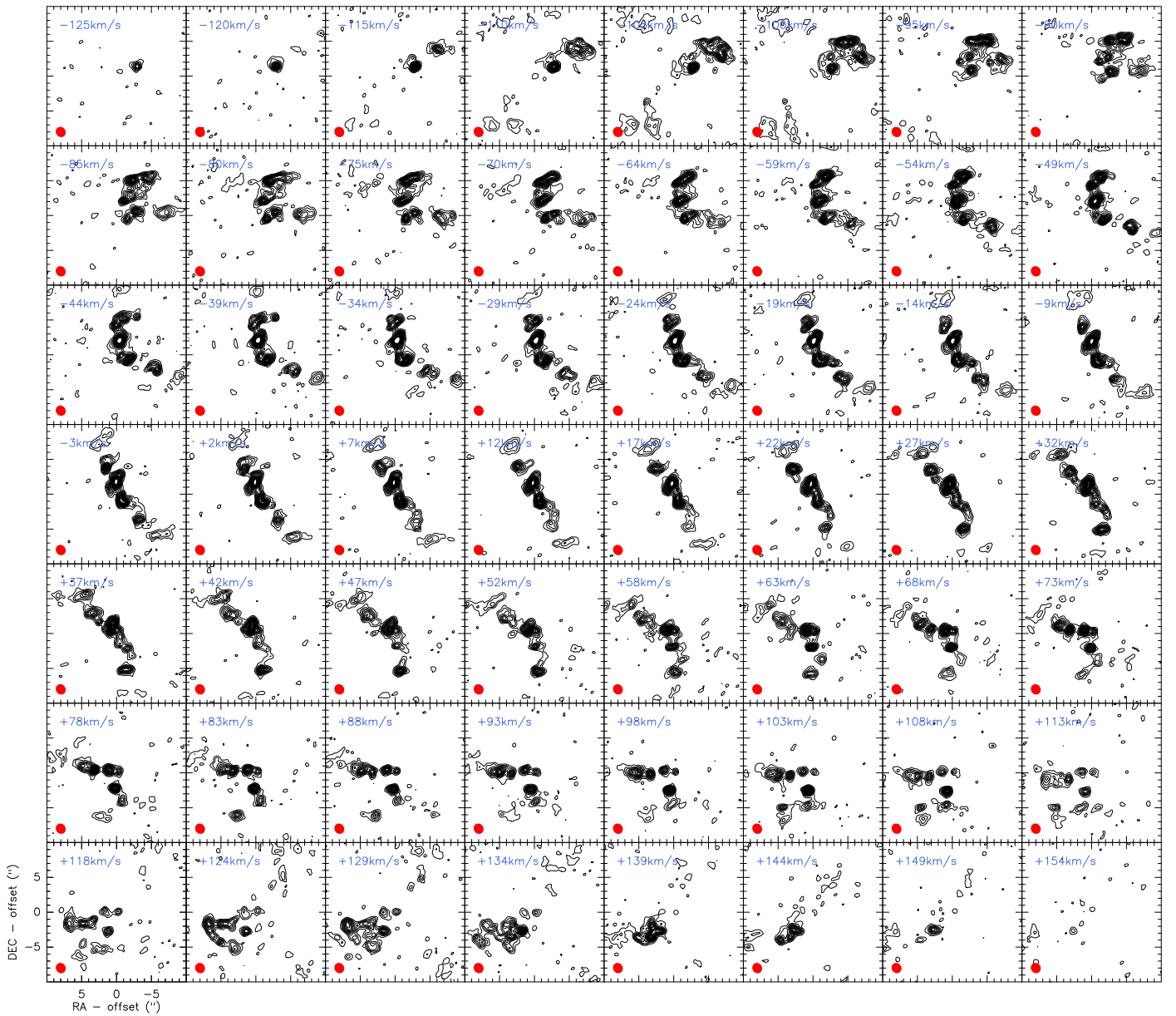
Figure 2. CO(2–1) emission channel maps in velocity bins of $\sim$5 km s^{-1}. Each box is 1.1 kpc on the side. The velocity of each map relative to the systemic one is indicated in the labels (the systemic velocity is taken equal to the LOS, $v_{\rm sys}$ = 1687 km s^{-1}). The synthetic beam is shown in the bottom-left corner by a red ellipse. Contours are 2σ to 40σ in steps of 2σ, σ = 1.16 mJy/beam.

L' CO$_{\rm red}$ = (6.6 ± 0.5) × 10^5 K km s^{-1} pc^2 and L' CO$_{\rm blue}$ = (1.3 ± 0.1) × 10^6 K km s^{-1} pc^2.

Figure 6 shows also spectra of the CNR, and of the nuclear equatorial gas lane (see the caption). The CNR shows projected velocities in the range of ±100 km s^{-1}, whereas the gas in the nuclear region reaches velocities of -120 and 150 km s^{-1}. We estimate the CO luminosity of the CNR into L' CO = 9.6 × 10^6 K km s^{-1} pc^2, and of the nuclear gas lane L' CO = 2.8 × 10^6 K km s^{-1} pc^2, by integrating the total flux density of the corresponding spectrum (i.e., the pink histogram, Figure 6).

3.2. Nuclear Region

To investigate the morphology and kinematics of the inner 1″ ($\sim$100 pc) region, we used the data cube with enhanced angular resolution (Section 2). Figure 7 (upper panels) shows the mean-flux, mean-velocity, and velocity dispersion maps within the inner 2.5 × 2″5 region around the AGN. Arc-like CO-emitting structures and gas lanes coming in from the CNR toward the AGN are detected. The inner equatorial CO(2–1) gas lane major axis is oriented approximately at PA = 125°, and is resolved into three main clumps. We modeled the emission in this region with tilted rings with fixed inclination (i = 60°) and PA = 125°. Figure 7 (lower panels) shows the model moment 0, 1, 2 maps, and the $data - model$ residual velocity map, the latter showing residual emission from redshifted gas at nucleus. The kinematic components giving rise to these residuals are also seen in the PV diagrams in Figure 8. The molecular gas kinematics shows evidence of an inner rotating disk (shown by red contours and yellow solid points), warped compared to the main outer disk, and of additional kinematic components with velocity up to about ±120 km s^{-1} along both directions within the inner arcsec.

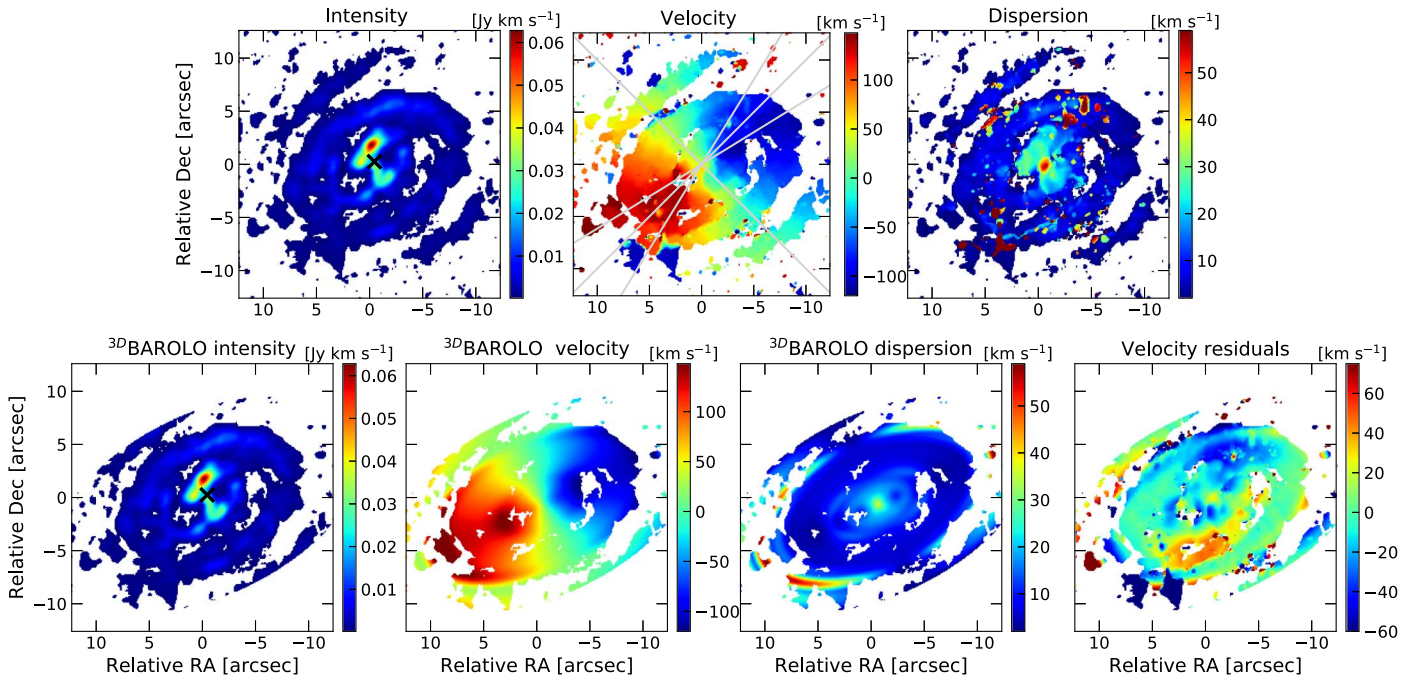**Figure 3.** Upper panels, left to right: the CO(2–1) intensity, mean-velocity, and velocity dispersion, σ_{disp}, maps derived from ALMA observations. A detection threshold of 3.5σ was applied to derive the moment maps. The cross indicates the position of the 1.3 mm continuum peak. The gray lines indicate the orientation of the slices used to derive the PV diagrams in Figure 5. Bottom panels, left to right: the mean-intensity, mean-velocity, and velocity dispersion maps of the ^{3D}BAROLO model of the disk, and the velocity residuals maps (i.e., data velocity map−model velocity map.)
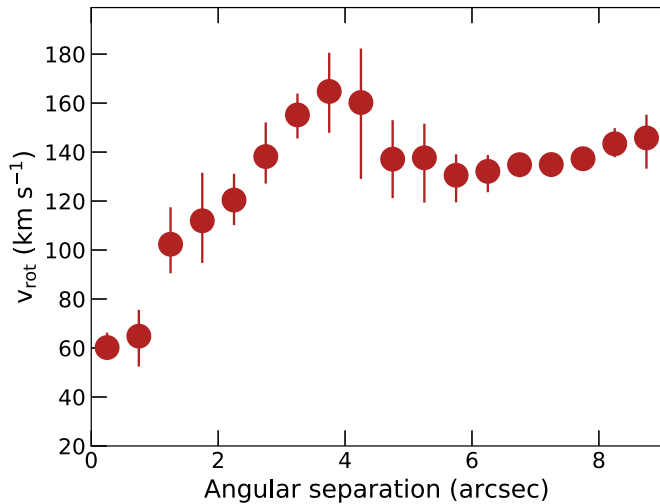
Figure 4. Rotation velocity v_{rot} vs. the radius of the best-fit inclined disk model derived by ^{3D}BAROLO. v_{rot} increases from the center, shows a peak between radii 2 and 4″, and then reaches a plateau at 135 km s^{-1} in the outer part of the disk.

We compare the distributions of the cold gas and dust emission seen in the ALMA data in the nuclear region, with that of the X-ray and H$_2$ emitting material detected with *Chandra* and SINFONI/VLT. Figure 9 shows color images in *Chandra* energy bands, over which contours of the 1.3 mm continuum, CO(2–1) and H$_2$ emission have been overplotted. The 1.3 mm continuum emission (green contours) peaks close to the X-ray nucleus and partly overlaps with the extended soft X-ray emission toward the southeast. Both the X-ray and 1.3 mm continuum in this region are distributed along a PA similar to that of the ionization cone and radio jet (Falcke et al. 1998), and 2.12 μm H$_2$-emitting gas (yellow contours, May et al. 2018).

The inner transverse CO gas lane overlaps with the most obscured, Compton-thick region seen in X-rays (Figure 7 in Fabbiano et al. 2018a, and Figure 9, lower right panel). The CO emission from the CNR partly overlaps with the hard band 3–6 keV emission, which, however, extends beyond the CO-emitting region. This configuration appears to form a CO-cavity, filled with X-ray emitting material and with H$_2$-emitting gas.

4. Discussion

4.1. Molecular Disk

We measure a molecular gas reservoir of $M(H_2) = 6.7 \times 10^7 (\alpha_{CO}/3.2) M_\odot$. However, it is difficult to exactly quantify the fraction of flux which may have been filtered out by the interferometer on large scales. The brightest CO emission is detected in a CNR with radius 200 pc and mass $M(H_2) = 3 \times 10^7 (\alpha_{CO}/3.2) M_\odot$. We interpret this structure as the inner Lindblad resonance region, in which, according to Combes & Gerin (1985), the gas can get stalled in ring-like structures, before being fed toward the nucleus.

Regarding the kinematics of the molecular gas in the host galaxy, most of the observed velocity gradient on large scales is well modeled with an inclined rotating disk seen at an inclination of $i = 60°$, and with $v_{rot} = 135$ km s^{-1}. Based on our modeling, we derive a dynamical mass $M_{dyn} = R \times v_{rot}^2/G = 5 \times 10^9 M_\odot$ within a radius of ~1 kpc.

The PV plot along the kinematic minor axis (Figure 5) shows deviations from a constant radial velocity. These wiggles recall similar features observed in other nearby galaxies like, e.g., NGC 1566 and NGC 1961 (Combes et al. 2009, 2014), NGC 4826 (Garcia-Burillo et al. 2003), NGC 3147 (Casasola et al. 2008), and NGC 3393 (Finlez et al. 2018), from the NUGA sample, that are generally interpreted as gaseous spiral and
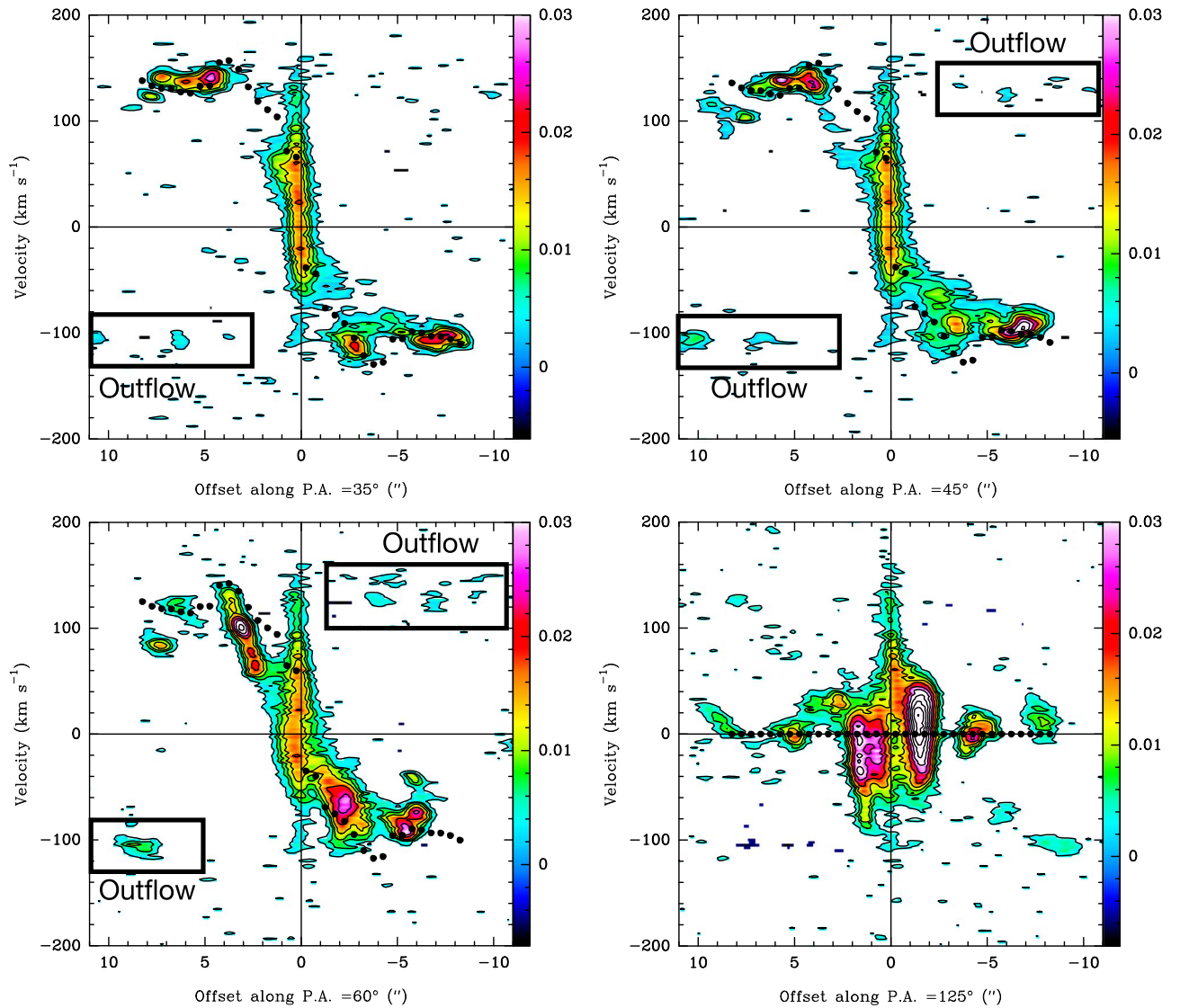
Figure 5. Set of position–velocity (PV) diagrams along different PA, selected to capture the different kinematic components seen in Figure 3. The orientation of each slice is marked in Figure 3 with gray lines. Upper panels: PV plot along PA = 35°(i.e., the kinematic major axis) and PA = 45°. Lower panels: PV plots along PA = 60° and PA = 125° (i.e., the kinematic minor axis). PA is defined positive starting from east counterclockwise. The slit width is set to 0″9 (i.e., approximately the FWHM size of the synthetic beam major axis). The contours are (2, 5, 10, 15, 20, 25, 30)σ, σ = 1.25 mJy/beam per 2.5 km s^{-1} channel. The black filled points show the projected rotational velocity of the disk model (Figure 3).

turbulent perturbations. We find that the $\sigma_{\mathrm{disp}}/v_{\mathrm{rot}}$ varies between ~0.1 in the spiral arms, 0.4–0.5 in the CNR and inner ~100 pc region.

We show in Figure 10 the [O III]λ5007 Å velocity and velocity dispersion map from MUSE (C. Feruglio et al. 2020, in preparation), which traces the distribution and kinematics of ionized gas in the host galaxy. [O III] shows a mean-velocity gradient with similar PA to that observed for CO. We note that the MUSE FOV is larger than the ALMA primary beam of these observations. The ionized gas traced by [O III] shows velocity dispersion reaching FWHM = ~150–180 km s^{-1} (Figure 10), corresponding to $\sigma_{\mathrm{disp, \,[O\,III]}} = 60$–$80$ km s^{-1} at the location of the outer CO arm, and exceeding $\sigma_{\mathrm{disp, \,[O\,III]}} \sim 100$ km s^{-1} in the CNR and nucleus. The regions with the largest [O III] velocity dispersion trace well the molecular spiral arms, CNR and inner gas lane.

4.2. Feeding

In the nuclear region, the two brightest portions of the CNR appear connected by a transverse gas lane (or inner bar), which goes through the nucleus. We estimate a mass of molecular gas in the inner bar of $M(\mathrm{H}_2) = 9 \times 10^6 (\alpha_{\mathrm{CO}}/3.2)\ M_\odot$ within a region of radius ~50 pc. In this inner region, we detect gas with projected velocity out to 150 and -130 km s^{-1} (Figures 4 and 8). The gas kinematics in this region show evidence of both rotation and of additional kinematic components which are not explained by our inner disk model, and which may lead to fueling of material toward the AGN.

It is possible that (part of) this fast gas has non-null angular momentum. If we assume that angular momentum is zero and the velocity is radially oriented, we can estimate an upper limit on the inflow rate within the nuclear region—keeping in mind that higher resolution data are required to obtain a better
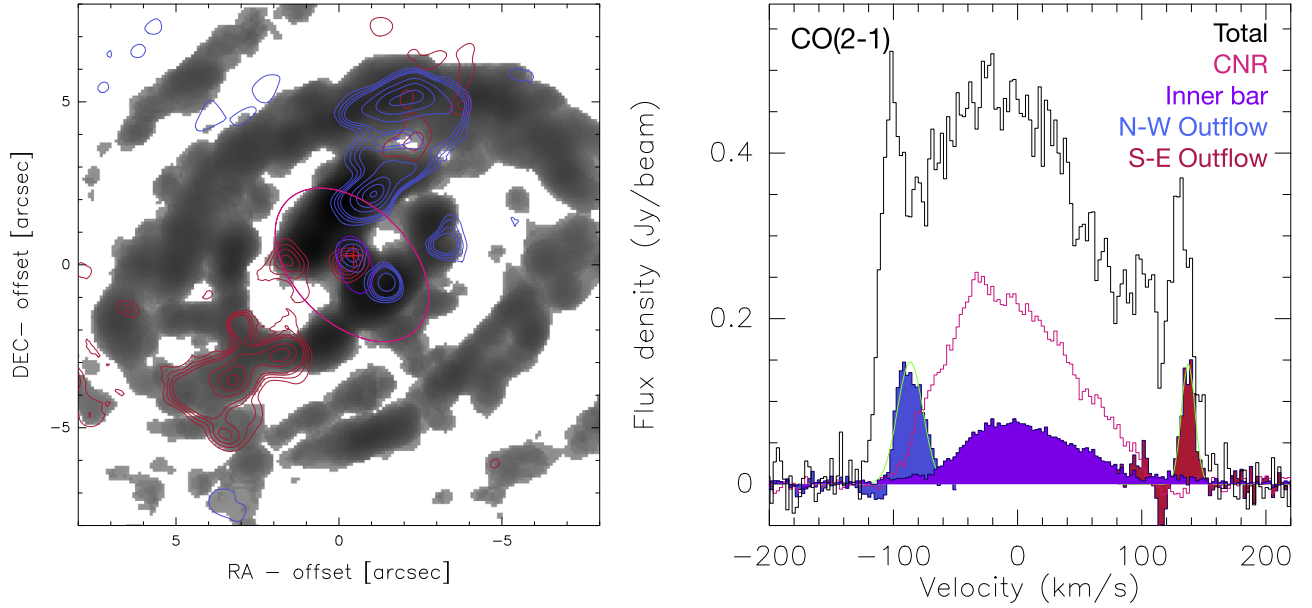
Figure 6. Left panel: the velocity-integrated CO(2–1) emission map (in grayscale, same as Figure 1). Blue and red contours show the velocity-integrated CO(2–1) residual emission, after subtraction of the disk rotation model of Figure 3 (lower panels). Contours levels are (2, 3, 4, 5, 10, 15, 20, 25, 30, 25)σ, $\sigma = 0.63$ mJy/beam for the blue and 0.8 mJy/beam for the redshifted component, respectively. Pink and purple ellipses show the regions from which we extracted spectra shown by the histograms in the right panel. Right panel: the continuum-subtracted CO(2–1) emission line extracted from different regions. Each histogram is color-coded according to the corresponding region shown in the legend and in the left panel. Black histogram: CO(2–1) spectrum of the galaxy extracted using a mask derived from the $>2\sigma$ region in Figure 1. Pink and purple histograms: CO(2–1) extracted from the CNR and nuclear equatorial bar. The extraction regions are indicated with pink and purple ellipses in the left panel, respectively. Blue and red histograms: CO(2–1) emission extracted from the regions enclosed by the blue and red contours in the left-hand map. The green solid lines indicate the Gaussian best fit to the emission lines.
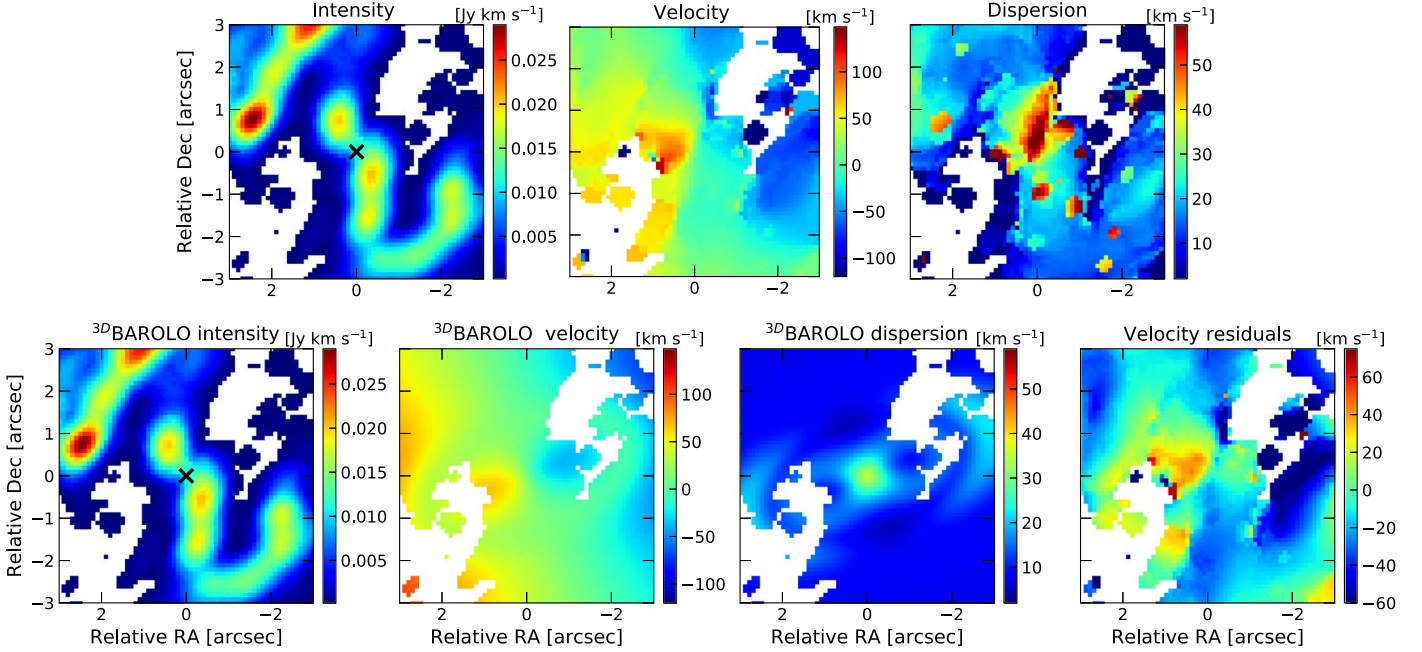

Figure 7. Top panels, left to right: the CO(2–1) mean-flux, mean-velocity, and velocity dispersion maps, derived for the inner $2\overset{''}{.}5 \times 2\overset{''}{.}5^2$ region from the high resolution data cube. Bottom panels, left to right: the ^{3D}BAROLO model mean flux, mean velocity, and velocity dispersion maps, and the residual mean-velocity field map. The cross indicates the position of the 1.3 mm continuum peak.

dynamical model of the inner 100 pc region. We note that inward radial motions do not imply that the gas actually fuels the AGN, as it may pile up in a nuclear ring before reaching the nucleus. In fact, observational evidences of inflows are still rare and challenging to achieve even in nearby galaxies (e.g., NGC 4579, Garcia-Burillo et al. 2009). The inflow rate is computed as $\dot{M}_{in} = v_{R_{in}} \times M(H_2)_{radial}/R_{in}$. We estimate the

inflow radius, R_{in}, from Figure 8, from which we see that most of this fast gas is located in the inner $0\overset{''}{.}5$. We adopt therefore $R_{in} = 60$ pc. We estimate the velocity of the inflowing gas, $v_{R_{in}}$, from the gas that exceeds the rotational velocity in Figure 8. At R_{in}, $v_{R_{in}} \approx 75$ km s^{-1}. The molecular inflowing mass $M(H_2)_{in}$ is estimated from the residual data cube, which in turn obtained subtracting the model in Figure 7 from the data. In the residual
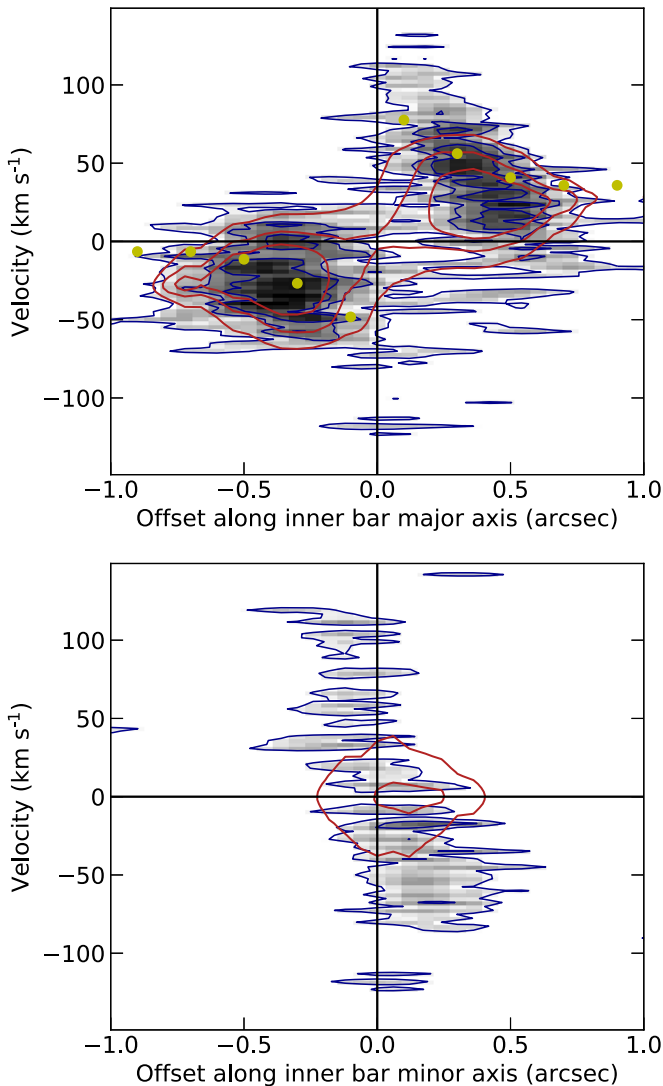
Figure 8. PV diagram of the nuclear region along the major axis of the inner CO bar (PA = 125°, upper panel), and along the minor axis (lower panel). Red contours and yellow points indicate the expectation for an inclined rotating disk with inclination 60°. Deviations from the rotation velocity are detected in the inner 1″, where molecular gas with velocity up to ±120 km s^{-1} is detected.

data cube we collapse the channels with velocity larger than ±75 km s^{-1} in the inner 0″5 region, and derive a velocity-integrated map from which we estimate L'CO. We find L'CO = 2.8$10^5$ K km s^{-1} pc^2. This translates into a molecular mass of $M(H_2)_{in}$ = 9 10^5 (α_{CO}/3.2) $M_\odot$, and in an inflow rate of $\dot{M}_{in} \approx 1\, M_\odot$ yr^{-1}.

The Bondi radius of the BH in ESO428–G14 is of the order of 1 pc, much smaller than the size of the inner gas lane; therefore, the molecular gas can undergo significant fragmentation and star formation before reaching the nucleus, if the dynamical timescale is longer than the star formation depletion timescale, $t_{dep} = M_{gas}$/SFR. We evaluate the SFR in the inner 100 pc from the 1.3 mm continuum flux density, and adopt the M82 spectral energy distribution. We compute the far-infrared luminosity of ESO428–G14 and convert it into a SFR < 0.3 $M_\odot$ yr^{-1}. This is a strict upper limit to the SFR because the 1.3 mm flux density has certainly a contribution from the AGN, although this cannot be quantified with the data in hand. Similarly, the narrow Hα luminosity in this central region derived from the MUSE data, can hardly be an SFR

indicator, because of the Narrow Line Region contribution. Based on our SFR upper limit, we derive a gas depletion timescale $t_{dep} = \epsilon_{SF} M_{gas}$/SFR > 3 Myr, where $\epsilon_{SF} \approx 0.1$ is the efficiency of gas conversion for star formation.

The dynamical timescale of the gas located at about 60 pc (0″5) from the AGN position is $t_{dyn} = R/v(R) \approx 0.8$ Myr, where $v(R) = 75$ km s^{-1} is the bulk radial velocity of the gas at $R = 60$ pc from Figure 8. Because $t_{dep} > t_{dyn}$, it is unlikely that all the inflowing molecular gas in the inner bar fuels nuclear star formation.

The BH accretion rate inferred from the bolometric luminosity L_{bol}, $\dot{M}_{BH} = L_{bol}/\epsilon c^2 = 0.007\, M_\odot$ yr^{-1} for a radiatively efficient accretion ($\epsilon = 0.1$), or 0.07 $M_\odot$ yr^{-1} for a radiatively inefficient accretion ($\epsilon = 0.01$). Even for the latter case, $\dot{M}_{BH} < \dot{M}_{in}$, suggesting that a large fraction of the gas within R_{in} does not reach the black hole. A possible solution is that a large fraction of the inflowing gas is lost in outflows (see Section 4.3), thus reducing the net accretion rate reaching the BH, $\dot{M}_{BH}$, as predicted for both radiatively efficient accretion flows (e.g., Kurosawa & Proga 2009) and radiatively inefficient flows (e.g., Yuan et al. 2015; Sadowski et al. 2016).

Interestingly, the inner CO bar overlaps with the most obscured, CT region seen in X-rays (Figure 7 in Fabbiano et al. 2018a, and Figure 9, lower right panel). We estimate the line-of-sight H$_2$ column density of $N(H_2) \approx 2 \times 10^{23}$ cm^{-2} toward the the inner bar region, which has approximate size of 100 by 50 pc^2. This is similar to the $N(H_2)$ found in other local Seyfert galaxies (Alonso-Herrero et al. 2018, 2019; Izumi et al. 2018), and smaller than the neutral hydrogen column density N_H toward the AGN, as derived from X-ray observations, which is >10^{24} cm^{-2} (Fabbiano et al. 2017, 2018b). This $N(H_2)$ is a lower limit of the true column density due to beam dilution. In addition, $N(H_2)$ is derived for a given conversion factor ($\alpha_{CO} = 3.2\, M_\odot$ K^{-1} (km s^{-1-1}) pc^2). While there is empirical evidence that in the nuclei of galaxies the conversion factor is smaller than the Milky Way (MW) value and can be of the order 1, there have also been claims that it can be a factor of a few higher than in the MW (e.g., Wada et al. 2018). The uncertainties on $M(H_2)$, and consequently on $N(H_2)$, are therefore of the order of a few. It is thus possible that the molecular nuclear gas contributes significantly to the Compton thickness of this AGN.

The nuclear equatorial lane may be identified with an inner bar, or with the (outer portion of the) molecular torus, similarly to what was found in NGC 5643 by Fabbiano et al. (2018c) and Alonso-Herrero et al. (2018). In that AGN, the nuclear molecular disk also matches the regions with the largest nuclear obscuration seen in X-rays. Higher angular resolution observations are required to confirm this scenario and map in detail the distribution and kinematics of molecular gas in the nucleus of ESO428–G14.

4.3. Feedback

The nuclear configuration of the CO and X-ray emitting gas in ESO428–G14 resembles the case of NGC 1068 as studied by Garcia-Burillo et al. (2010). They found that hard X-ray emission overlaps with the molecular circumnuclear disk, but also extends further out from it, like in the case of ESO428–G14. These CO cavities are puzzling because the hard (3–6 keV) continuum and Fe Kα emission require scattering from dense neutral clouds in the ISM (Fabbiano et al. 2018c), therefore we would expect to detect CO in the region detected
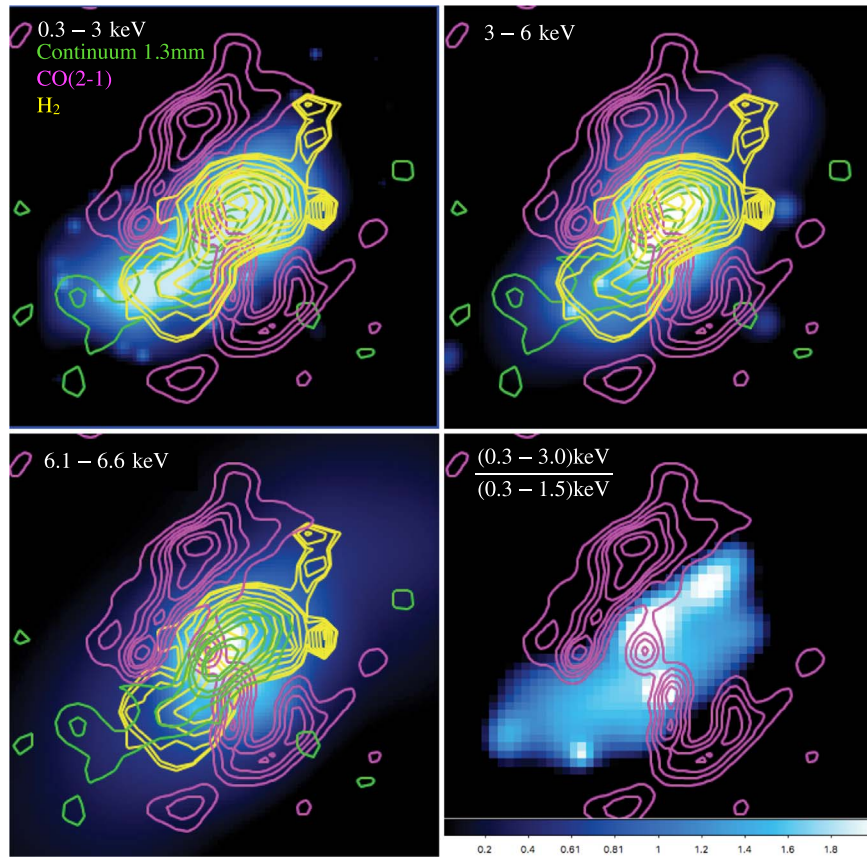
Figure 9. Zoom-in toward the nuclear region of ESO428–G14. Color images are the *Chandra* soft (upper left panel), hard band (upper right panel), and Fe Kα line emission (lower left panel), and hardness ratio (0.3–3.0 keV)/(0.3–1.5 keV) maps (from Fabbiano et al. 2018c). Green contours = 1.3 mm continuum detected by ALMA imaged with robust weighting. Magenta contours = velocity-integrated CO(2–1) line emission imaged with robust weighting to enhance the angular resolution in the nuclear region. Yellow contours = warm molecular gas traced by the H_2 2.12 μm line from SINFONI/VLT data.
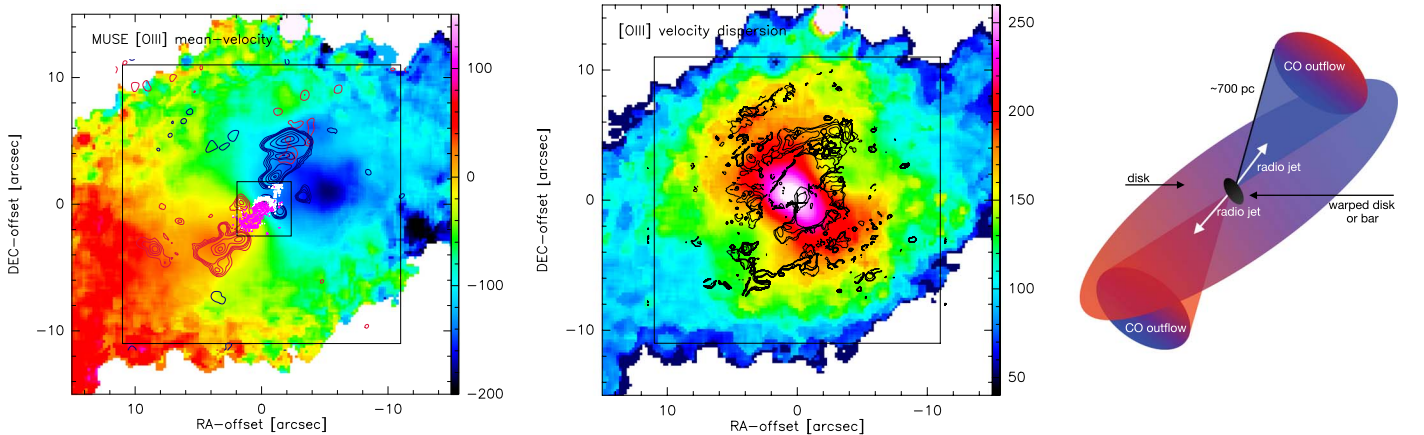

Figure 10. Left panel: [O III]λ5007 Å mean-velocity map of ESO428–G14 obtained with MUSE/VLT. The PSF of MUSE data is 1″.2. Red/blue contours = receding/approaching CO outflow. Contours are as in Figure 6. White/magenta contours = receding/approaching sides of the H_2 emission line from SINFONI data. The outer box shows the 22″ × 22″ field of view shown in Figure 3. The inner square shows the SINFONI field of view based on May et al. (2018) data. Middle panel: the [O III] velocity dispersion map ($\sigma_{disp,[O III]}$). Overplot with black contours is the CO(2–1) mean velocity dispersion map, levels are 10, 20, 30, 40, 50 60, 70, 80, 90, and 100% of the maximum velocity dispersion. Color scale units are km s^{-1}. Right panel: a sketch of the ESO428–G14 disk, outflow, and jet. The color palette indicates blue–redshifted velocity. The CO disk and outflow are derived from ALMA observations. White arrows indicate the approximate orientation of the radio jets found by Falcke et al. (1998). The gray ellipse indicates the innermost region, which may be a warped disk or bar.

in hard X-ray in ESO428–G14. The upper limit derived from these observations implies that the mass of molecular gas in such dense clouds must be smaller than $M(H_2) < 7 \times 10^5 (\alpha_{CO}/3.2) M_\odot$. It is possible that in this region CO(2–1) emission is suppressed due to strong AGN irradiation and/or shocks. The detection of warm molecular gas traced by the

H_2 2.12 μm emission line in the CO cavity supports this scenario, confirming that the scattering material giving rise to the hard X-ray extended emission is warm molecular gas, as suggested by Fabbiano et a. (2018). A similar case of X-ray and warm H_2-emitting gas filling a CO-deprived region, has been reported in the AGN host galaxy NGC 2110 by

Fabbiano et al. (2019) and Rosario et al. (2019), whereas Shimizu et al. (2019) find a CO and warm H_2-deprived region around the nucleus of a AGN with higher L_{bol}, NGC 5728. Kawamuro et al. (2019) also report a spatial anticorrelation of the iron Kα emission and the location of dense molecular clouds in the Circinus galaxy. In ESO428–G14, CO may be excited to higher excitation levels up the CO ladder in this region, due to irradiation by hard X-ray field and/or shocks.

At larger distances from the nucleus, several kinematic disturbances are detected in the mean-velocity and velocity dispersion maps, which indicate outflowing gas. The PV diagrams along PA = 45 and 60° (Figure 5) show that several clumps of nonrotating molecular material are detected at projected distances of $\sim 2''$–$7''$ (i.e., 0.2–0.7 kpc) from the AGN with projected velocities $v_{out} = +130$ and $-110\,\mathrm{km\,s^{-1}}$. Figures 2, 3, and 6 (inset) show that these clumps are distributed in a biconical pattern. Because the PA of the outflow is similar to that of the main velocity gradient of the disk and spiral arms, in the outer parts the outflow overlaps with the rotation pattern in both space and velocity, making it challenging to separate the rotation of the main disk from the outflow. The apparent counter-rotation seen in PV diagrams along PA = 35, 45, and 60°, confirms that these components trace the two sections of a biconical outflow.

The projected distance reached by the outflow is about 700 pc on both sides of the AGN. The mass of molecular gas in the two cones is estimated using the conversion factor α_{CO} for both the case of optically thin gas (e.g., Dasyra et al. 2016; Morganti et al. 2015), and for optically thick gas. For optically thin gas, $\alpha_{CO} = 0.3\,M_\odot\,[\mathrm{K\,km\,s^{-1}\,pc^2}]^{-1}$, and for the optically thick case $\alpha_{CO} = 0.8\,M_\odot\,[\mathrm{K\,km\,s^{-1}\,pc^2}]^{-1}$ is a conversion factor often used for molecular outflows (Bolatto et al. 2013; Morganti et al. 2015). These imply outflow masses of $M(H_2)_{blue} = 2$–$5 \times 10^5\,M_\odot$ and $M(H_2)_{red} = 4$–$10 \times 10^5\,M_\odot$, for the optically thin/thick case of the blue and red component, respectively.

We derive the outflow rate through the relation

$$\dot{M}_{of} = \frac{M_{of}\,v_{out}}{R_{of}} \qquad (1)$$

where the outflow projected velocity is $v_{out} = -100\,\mathrm{km\,s^{-1}}$ and $v_{out} - = 130\,\mathrm{km\,s^{-1}}$ (Figure 5), on the blue and red sides, respectively, and we add up the contributions of both cones. We find a molecular outflow rate in the range $\dot{M}_{of} \approx 0.1$–$0.3\,M_\odot\,\mathrm{yr^{-1}}$, for the optically thin and thick cases, respectively. The escape velocity at a radius of 1 kpc is $v_{esc} = \sqrt{(G\,M_{dyn}/R)} = 150\,\mathrm{km\,s^{-1}}$. Because $v_{out} \approx v_{esc}$, it is likely that at least part of the outflowing gas does not leave the galaxy but eventually rains back onto the disk.

We find regions of enhanced CO velocity dispersion in the disk along the direction of the CO outflow and ionization cone, suggesting that the outflow injects turbulence in the interstellar medium. The CO data suggest that the molecular outflow is launched at a small inclination with respect to the disk plane, as are the radio jet and the [O III] outflow (Falcke et al. 1996; Riffel et al. 2007). It is likely that the radio jet and ionized outflow impact the disk, thus lifting-up molecular material from the galactic plane.

In Figure 10 we show the MUSE [O III] velocity map. We overplot CO outflow emission (blue/red contours) and the H_2 2.12 μm line emission derived from SINFONI data (white and magenta contours). May et al. (2018) detected a nuclear

outflow using the [Si VI] $\lambda 19641$ Å coronal line from the same SINFONI data set, and they estimated an outflow rate of warm molecular gas of $\dot{M}_{H_2,warm} = 3 - 8\,M_\odot\,\mathrm{yr^{-1}}$ within the central 170 pc region (with outflow reaching a projected distance of about ~ 65 pc from the AGN). We show in Figure 10 that the cold CO and the H_2 warm outflows appear to join smoothly with one another, and both are approximately aligned with the [O III] ionization cone and radio jet direction. The warm H_2 outflow traces the inner portion of the outflow detected in CO, suggesting that the outflow may cool with increasing distance from the AGN. However, SINFONI FOV covers only the inner $3''$ region, therefore with the data in hand we cannot exclude that the warm H_2 outflow extends also further out. A complete analysis of the [O III] kinematics, separating and modeling the contribution of the host galaxy rotating disk from the AGN ionization cones and outflows, will be presented in Paper II (C. Feruglio et al. 2020, in preparation), and will provide constraints to the multiphase properties of the ISM in the disk and outflow.

5. Conclusions

We imaged the molecular gas of the host galaxy of the nearby CT AGN ESO428–G14 at ~ 80 pc resolution using ALMA archival data of CO(2–1) line and 230 GHz continuum. We joined ALMA data with *Chandra* X-ray data, MUSE/VLT [O III] and H_2 2.12 μm maps from SINFONI/VLT, and derived the following conclusions.

1. The CO emission is distributed in clumpy spiral arms out to radii of about 1 kpc, in a lopsided CNR with ~ 200 pc radius, and in a transverse gas lane with size of <100 pc, which crosses the nucleus and connects the two brightest portions of the CNR. The brightest CO emission is detected in the CNR, for which we estimate a molecular mass of $M(H_2) = 3 \times 10^7 (\alpha_{CO}/3.2)\,M_\odot$. We interpret the CNR as the inner Lindblad resonance region, in which the gas can get stalled in ring-like structures, before being fed toward the nucleus. Our dynamical modeling is consistent with a rotating disk inclined at $i \sim 60°$, and with $v_{rot} = 135\,\mathrm{km\,s^{-1}}$. We derive a dynamical mass $M_{dyn} = 5 \times 10^9\,M_\odot$ within a radius of ~ 1 kpc.

2. In the inner 100 pc region, our dynamical modeling suggests the presence of a warped disk or bar, and of additional fast gas streams, the latter suggestive of an inflow of material toward the nucleus with a rate of $\dot{M}_{in} \approx 1\,M_\odot\,\mathrm{yr^{-1}}$. Observations with angular resolution of ~ 10 pc are required to achieve a better dynamical model of this inner region. The inner CO bar/warped disk overlaps with the most obscured, Compton-thick region seen in X-rays, and with its estimated column density of $N(H_2) \approx 2 \times 10^{23}\,\mathrm{cm^{-2}}$, may contribute significantly to the Compton thickness of this AGN as measured by X-ray observations.

3. We detect a molecular outflow with a rate of $\dot{M}_{of} = 0.1 - 0.3\,M_\odot\,\mathrm{yr^{-1}}$, distributed along a biconical structure with projected size of ~ 700 pc on both sides of the AGN, approximately along the direction of the [O III] ionization cones, and along the same direction of the H_2 outflow reported by May et al. (2018), and of the radio jet reported by Falcke et al. (1998). The warm molecular outflow traced by H_2 is detected in the inner 170 pc,

whereas the CO outflow is detected out to 700 pc, possibly indicating that the gas cools while leaving the nucleus. We find regions of enhanced CO velocity dispersion in the disk along the direction of the CO outflow and ionization cones, suggesting that the outflow injects turbulence in the interstellar medium. It is possible that the CO outflow is the result of the AGN wind, either the warm H_2 or the [O III] ionized winds, impacting the disk and lifting-up molecular material from the disk plane. This mechanism could explain the fact that the disk rotation velocity and the outflow velocity are similar. We find that the CO outflow velocity is of the same order as the escape velocity, $v_{out} \approx v_{esc}$, suggesting that at least part of the outflowing gas does not leave the galaxy but eventually rains back onto the disk.

4. The hard band 3–6 keV X-ray emission partly overlaps with the molecular CNR, but extends further out, and in particular it is detected in the CO-deprived region (CO-cavity). We find that the CO-cavity is filled with warm molecular gas, traced by the 2.12 μm H_2 emission line. This confirms that the hard (3–6 keV) continuum and Fe Kα emission are due to scattering from dense neutral clouds in the ISM. This region hence contains molecular material, but may appear CO-deprived due to irradiation by the AGN hard X-ray field and/or shocks, which may excite CO to higher levels up the rotational ladder. Observations of higher J CO transitions may be useful to map the molecular gas and constrain the effects of AGN feeding and feedback in the inner nuclear region.

ORCID iDs

C. Feruglio https://orcid.org/0000-0002-4227-6035
G. Fabbiano https://orcid.org/0000-0002-3554-3318
M. Bischetti https://orcid.org/0000-0002-4314-021X
M. Elvis https://orcid.org/0000-0001-5060-1398

References

Accurso, G., Saintonge, A., Catinella, B., et al. 2017, MNRAS, 470, 4750
Alonso-Herrero, A., Garcia-Burillo, S., Pereira-Santaella, M., et al. 2019, A&A, 628, A65
Alonso-Herrero, A., Pereira-Santaella, M., Garcia-Burillo, S., et al. 2018, ApJ, 859, 144
Bolatto, A. D., Wolfire, M., & Leroy, A. K. 2013, ARA&A, 51, 207
Borisova, E., Cantalupo, S., Lilly, S. J., et al. 2016, ApJ, 831, 39
Casasola, V., Combes, F., Garcia-Burillo, S., et al. 2008, A&A, 490, 61
Combes, F., Baker, A. J., Schinnerer, E., et al. 2009, A&A, 503, 73
Combes, F., Garcia-Burillo, S., Casasola, V., et al. 2014, A&A, 565, A97
Combes, F., & Gerin, M. 1985, A&A, 150, 327C
Dasyra, K., et al. 2016, A&A, 595, L7
Di Teodoro, E. M., & Fraternali, F. 2015, MNRAS , 451, 3021
Evans, I. N., Primini, F. A., Glotfelty, K. J., et al. 2010, ApJS, 189, 37E
Fabbiano, G., Elvis, M., Paggi, A., et al. 2017, ApJ, 842, 4
Fabbiano, G., Paggi, A., & Elvis, M. 2019, ApJL, 876, L18
Fabbiano, G., Paggi, A., Karovska, M., et al. 2018a, ApJ, 855, 131
Fabbiano, G., Paggi, A., Karovska, M., et al. 2018b, ApJ, 865, 83
Fabbiano, G., Paggi, A., Siemiginowska, A., & Elvis, M. 2018c, ApJ, 869, 36
Fabbiano, G., Siemiginowska, A., Paggi, A., et al. 2019, ApJ, 870, 69F
Falcke, H., Wilson, A. S., & Simpson, C. 1998, ApJ, 502, 199
Falcke, H., Wilson, A. S., Simpson, C., & Bower, G. A. 1996, ApJL, 470, L31
Finlez, C., Nagar, N. M., Storchi-Bergmann, T., et al. 2018, MNRAS, 479, 3892
Garcia-Burillo, S., Combes, F., Hunt, L. K., et al. 2003, A&A, 407, 485
Garcia-Burillo, S., Fernández-García, S., Combes, F., et al. 2009, A&A, 496, 85
Garcia-Burillo, S., Usero, A., Fuente, A., et al. 2010, A&A, 519, A2
Guilloteau, S., & Lucas, R. 2000, ASPC, 217, 299
Izumi, T., Wada, K., Fukushige, R., et al. 2018, ApJ, 867, 48
Kawamuro, T., Takuma, I., & Imanishi, M. 2019, PASJ, 71, 68
Kurosawa, R., & Proga, D. 2009, MNRAS, 397, 1791
Levenson, N. A., Heckman, T. M., Krolik, J. H., Weaver, K. A., & Zycki, P. T. 2006, ApJ, 648, 111
Maiolino, R., Salvati, M., Bassani, L., et al. 1998, A&A, 338, 781
May, D., Rodriguez-Ardila, A., Prieto, M. A., et al. 2018, MNRAS, 481, L105
McConnell, N. J., & Ma, C.-P. 2013, ApJ, 764, 184
McGaugh, S. S., & Schombert, J. M. 2014, AJ, 148, 77
McMullin, J. P., Waters, B., Schiebel, D., Young, W., & Golap, K. 2007, in ASP Conf. Ser. 376, Astronomical Data Analysis Software and Systems XVI, ed. R. A. Shaw, F. Hill, & D. J. Bell (San Francisco, CA: ASP), 127
Morganti, R., Oosterloo, O., Oonk, R., et al. 2015, A&A, 580, A1
Peng, C. Y., Impey, C. D., Ho, L. C., et al. 2006, ApJ, 640, 114
Riffel, R. A., Storchi-Bergamnn, T., Winge, C., & Barbosa, F. K. B. 2007, MNRAS, 373, 2R
Risaliti, G., Maiolino, R., & Salvati, M. 1999, ApJ, 522, 157
Rosario, D. J., Togi, A., Burtscher, L., et al. 2019, ApJL, 875, L8
Sadowski, A., Lasota, J.-P., Abramowicz, M. A., & Narayan, R. 2016, MNRAS, 456, 3915
Saintonge, A., Kauffmann, G., Kramer, C., et al. 2011, MNRAS, 415, 32
Shimizu, T., Davies, R., Lutz, D., et al. 2019, MNRAS, 490, 5860
Vaddi, S., O'Dea, C. P., Baum, S. A., et al. 2016, ApJ, 818, 182
Wada, K., Yonekura, K., & Nagao, T. 2018, ApJ, 867, 49
Wakker, B. P., & Schwarz, U. J. 1988, A&A, 200, 312
Yuan, F., Gan, Z., Narayan, R., et al. 2015, ApJ, 804, 101